

# Influence of the Radial Electric Field on the Shearless Transport Barriers in Tokamaks

F.A.Marcus<sup>1</sup>, M. Roberto<sup>1</sup>, I. L. Caldas<sup>2</sup>, K. C. Rosalem<sup>1</sup>, Y. Elskens<sup>3</sup>

<sup>1</sup>*Departamento de Física, Instituto Tecnológico da Aeronáutica, São José dos Campos, SP 1228-900, Brazil.*

<sup>2</sup>*Instituto de Física, Universidade de São Paulo, São Paulo, SP 05315-970, Brazil. and*

<sup>3</sup>*Aix-Marseille Université, UMR 7345 CNRS, campus Saint-Jérôme,  
case 321, av. esc. Normandie-Niemen, FR-13397 Marseille cedex 20*

(Dated: 08/10/2018)

In tokamaks, internal transport barriers, produced by modifications of the plasma current profile, reduce particle transport and improve plasma confinement. The triggering of the internal transport barriers and their dependence on the plasma profiles is a key nonlinear dynamics problem still under investigation. We consider the onset of shearless invariant curves inside the plasma which create internal transport barriers. A non-integrable drift-kinetic model is used to describe particle transport driven by drift waves and to investigate these shearless barriers onset in tokamaks. We show that for some currently observed plasma profiles shearless particle transport barriers can be triggered by properly modifying the electric field profile and the influence of non-resonant modes in the barriers onset. In particular, we show that a broken barrier can be restored by enhancing non-resonant modes.

## CONTENTS

I.	Introduction	2
II.	Drift Wave Transport model	3
III.	Shearless Transport barriers	4
IV.	Non Resonant Mode Amplitude	6
V.	Influence of the Electric Field Profile	7
VI.	Conclusions	8
	Acknowledgments	9
	References	9

## I. INTRODUCTION

The plasma confinement in tokamaks is limited by particle transport induced by the electrostatic turbulence [1]. For some discharges, internal transport barriers reduce this transport and improve the plasma confinement [2]. Experiments show that such barriers appear by modifications of the current profile using external heating and current drive effects [3]. In fact, besides the recent progress to understand this dependence [1], the triggering of internal transport barriers and their dependence with the plasma profiles still remain a central question to be better understood [3–5].

Much research has been done on the nature of the transport barrier in high confinement mode discharges, in a number of tokamaks worldwide, and the influence of radial electric fields on the particle transport in magnetically confined fusion plasmas is by now well established [6]. Specifically, measurements of the radial electric field indicate that the negative shear region of the  $E_r$  profile plays a key role in turbulence reduction observed in H-mode, paving the way towards an improved understanding of the pedestal structure [6]. So, high-accuracy characterization of the edge radial electric field can be used to validate transport theory and identify the onset of transport barriers [6, 7]. In this context, the  $\mathbf{E} \times \mathbf{B}$  shear stabilization effect has been considered to be the origin of transport barriers identified in tokamaks [8].

On the other hand, the onset of shearless invariant curves inside the plasma could be a factor responsible for the formation of some internal transport barriers [9, 10]. In fact, these curves act as dikes preventing chaotic particle transport across them, and so are identified as a kind of shearless transport barrier. The essentials of a system with shearless transport barriers are exhibited by a simple symplectic two-dimensional mapping called standard non-twist map [11]. As shown in Ref. [12] for this map, even after the invariant surfaces have been broken, the remnant islands may present a large stickiness that reduces the transport.

Concerning the context of particle transport in tokamaks, the onset of these shearless barriers has been proposed to explain the reduction of transport in tokamaks [13] and helimaks [14]. In fact, in [13], for large aspect ratio tokamaks, a non-integrable drift model has been proposed to interpret the high particle transport at the plasma edge as being induced by the electrostatic turbulence, as caused by the  $\mathbf{E} \times \mathbf{B}$  chaotic radial drift motion of particles. Furthermore, this model has been applied to identify particle barriers in tokamak experiments [10, 15].

The model introduced in [13] is applied to show that, for some currently observed plasma profiles, shearless particle transport barriers can be triggered by alterations on the plasma profiles. These barriers can appear due to modes present in the turbulence, and the resonant conditions are determined by the combination of the safety factor, electric radial field component and the plasma toroidal velocity profiles. These profiles determine, respectively, the magnetic, radial electric field and plasma toroidal velocity shears, which are the relevant control parameters to specify the resonant condition. We show that enhancing non-resonant waves amplitude may restore shearless barriers while the resonant modes increase the particle chaotic transport. We also present examples for which the chaotic particle transport is reduced by the barrier onset due to slightly modifying the plasma parameters or even increasing the turbulence level.

In Section II, we introduce the drift wave transport model used in the article. In Section III, we present the equilibrium profiles and plasma parameters assumed in this article, and how the transport barriers are formed. In Sections IV and V, we analyze numerically the influence of the electric field profile and non-resonant modes on the barrier formation.

## II. DRIFT WAVE TRANSPORT MODEL

The model is based on equations of motion that describe particle trajectories following the magnetic field lines and the electric drift [13]. The particles trajectories are described by the guiding-center equation of motion

$$\frac{d\mathbf{x}}{dt} = v_{\parallel} \frac{\mathbf{B}}{B} + \frac{\mathbf{E} \times \mathbf{B}}{B^2} \quad (1)$$

giving the system of equations,

$$\begin{aligned} \frac{dr}{dt} &= -\frac{1}{rB} \frac{\partial \tilde{\phi}}{\partial \theta} \\ \frac{d\theta}{dt} &= \frac{v_{\parallel}}{r} \frac{B_{\theta}}{B} + \frac{1}{rB} \frac{\partial \tilde{\phi}}{\partial r} - \frac{E_r}{rB} \end{aligned} \quad (2)$$

$$\frac{d\varphi}{dt} = \frac{v_{\parallel}}{R}$$

where  $\mathbf{x} = (r, \theta, \varphi)$  is written in local polar coordinates standing  $r$  the radial position,  $\theta$  and  $\varphi$  the poloidal and toroidal angles,  $R$  is the major plasma radius,  $v_{\parallel}$  is the toroidal velocity of the guiding centers and  $E_r(r)$  is the radial electric field profile in equilibrium.

We consider an electric field composed of a radial mean part and a fluctuating part. Many experiments have shown the simultaneous excitation of a large spectrum of frequencies  $n\omega_0$ ,  $n = 1, 2, \dots, N$ , so the radial electric field of the fluctuating part appears as a wave spectrum given by [13],

$$\tilde{\phi}(\mathbf{r}, t) = \sum_{L, M, n} \phi_{LMn} \cos(M\theta - L\varphi - n\omega_0 t + \alpha_n) \quad (3)$$

where  $\tilde{\phi}$  is the fluctuating electrostatic potential such that  $\tilde{\mathbf{E}} = -\nabla \tilde{\phi}$ . The spatial electrostatic mode numbers  $L$  and  $M$  (respectively toroidal and poloidal) are assumed to be constant and  $\alpha_n$  are constant phases that do not affect the resonant conditions introduced later on.

The magnetic configuration is described by the safety factor  $q(r)$ , considering that  $B \approx B_{\varphi} \gg B_{\theta}$ , which corresponds to a layer of a large aspect ratio tokamak as in TCABR tokamak ( $a/R \simeq 0.3$ ), where  $a$  is the plasma radius. Therefore, the safety factor is calculated as  $q(r) = \frac{rB_{\varphi}}{RB_{\theta}}$ .

The differential equations (2) were normalized by taking  $a$ ,  $B_0$  and  $E_0$  as characteristic length scale, toroidal magnetic field and mean radial electric field at the plasma edge. To represent the results in Poincaré sections, we define a normalized action variable  $I \equiv (r/a)^2$  and angle variable  $\psi_{LM} \equiv M\theta - L\varphi$ , reducing the system of Eqs.(2) to the canonical pair  $(I, \psi)$ . Thus, for the normalized variables, the equations of motion are written as

$$\frac{dI}{dt} = 2M \sum \phi_n \sin(\psi - n\omega_0 t + \alpha_n) \quad (4)$$

$$\frac{d\psi}{dt} = \frac{v_{\parallel}(I)}{R} \frac{1}{q(I)} [M - Lq(I)] - \frac{M}{\sqrt{I}} E_r(I) \quad (5)$$

Without the fluctuating potential,  $\phi_n = 0$ ,  $I$  is a constant of motion and the system of equations (4) and (5) is integrable. The perturbation term consists of a sum of resonant drift waves, so, for a given wave spectrum, the system is quasi-integrable and its numerical solutions can be analyzed in phase space  $(I, \psi)$ . These solutions give the particle trajectories in phase space typical of quasi-integrable systems: regular, KAM invariants and islands, and chaotic trajectories [16]. The main resonances can be identified by the islands in phase space. We can analytically predict the position of primary resonances in phase space by examining Eq. (4), namely, the resonance location gives the action  $I$  where the wave modes are resonant. The resonances locations are determined by the action profiles of  $v_{\parallel}(I)$ ,  $q(I)$  and  $E_r(I)$  and by the wave numbers  $M$ ,  $L$ .

The islands in the Poincaré maps can be explained by taking the resonance conditions, which state to the time invariance of the action variable in Eq. (5), viz.  $\frac{d}{dt}(\psi - n\omega_0 t) = 0$ . Then, the resonance condition is obtained when

$(d\psi/dt)/\omega_0$  assumes values of the time mode  $n$  in Eq. (5), which determines the resonant action  $I_n$ :  $n = \frac{1}{\omega_0} \frac{d\psi}{dt}$ . Taking  $\frac{d\psi}{dt} = n\omega_0$  and inserting into Eq. (5) yields the value of  $I$  in which the frequency  $n\omega_0$  is resonant. So,

$$n\omega_0 = \frac{v_{\parallel}(r)}{R} \frac{1}{q(I)} [M - Lq(I)] - \frac{M}{\sqrt{I}} E_r(I) \quad (6)$$

In the next sections, particle trajectories are obtained by Bulirsch-Stoer numerical scheme [17] and their intersections in Poincaré sections are shown in  $(I, \psi)$  planes. We obtain a Poincaré map by integrating Eqs (4) and (5) for various initial conditions. The intersections of the integrated trajectories are selected at the toroidal section corresponding to instants  $t_j = j 2\pi/\omega_0$  ( $j = 0, 1, 2, \dots$ ). In Poincaré maps, the (nominal) minor plasma radius lies at  $I = 1.0$ , but we choose  $I$  up to 1.4 in order to investigate the particle transport to the chamber wall.

### III. SHEARLESS TRANSPORT BARRIERS

In general, a shearless transport barrier in a two-dimensional dynamical system is an invariant curve inside a set of invariant closed curves characterized by a non-monotonical canonical frequency profile. The shearless barrier corresponds to a quasi-periodic trajectory with a local extremum frequency [18]. Numerical studies show that the main feature of the shearless barrier compared with other KAM tori is that such barriers are more robust under time-periodic perturbations [11, 19]. This kind of barrier appears in the model considered in this work and has a dependence on the plasma profiles. Shearless barriers have been well described in the canonical Hamiltonian systems [11, 20, 21], adopted to present this barrier in the chaotic particle transport in tokamaks.

In our model, for null perturbing amplitude waves,  $\phi_n = 0$ , the system is integrable, each trajectory is periodic or quasi-periodic and stays in an invariant line with the initial action  $I_0$  constant. In this case, for each iterate in the Poincaré map, the associated helical angle  $\psi$  increases by a constant  $\Omega_0 = \Delta\psi$ , defined as the rotation number, which characterizes the invariant line.

In general, for non-vanishing  $\phi_n$ , we have a mixed system with chaotic trajectories and regular trajectories in invariant lines. In that sense, the rotation number profile can be an indicator of the behavior of the trajectories in any region of the phase space. For the non-integrable case, we can still define a rotation number for the remaining invariant lines, considering an initial condition  $\psi_0$ , as the limit  $\Omega = \lim_{i \rightarrow \infty} (\psi_i - \psi_0)/i$ , where  $\psi_i$  refers to the  $i$ -th section.

To determine the rotation number profile of the remaining invariant lines, we calculate the invariant rotation number, i.e., the limit  $\Omega$ , for initial conditions with a fixed angle variable  $\psi_0$  and a sequence of action variables  $I$ . If this profile shows an extremum, i.e.,  $d\Omega/dI \cong 0$ , the point  $(I, \psi_0)$  is a point in a shearless invariant. In this case, a shearless invariant curve appears in the phase space keeping the chaotic trajectories separated in two unconnected domains. The indicated shearless invariant curve acts as a barrier separating the particle orbits in the phase space and reducing the particle transport, thus, this shearless curve acts as an internal transport barrier. Even if this barrier is broken by perturbing waves, we expect from other maps analyses that the chaotic orbits may present a large stickiness around the remaining islands, which reduces the transport [19].

The existence and location of shearless barriers depend on the  $q(I)$ ,  $v_{\parallel}(I)$  and  $E_r(I)$  profiles, which are displayed in Fig.1a, 1b and 1c, respectively. These profiles are chosen similar to those observed in the small tokamak TCABR [7, 22], but our results can be applied to any tokamak described in a large aspect ratio approximation. To show how the shear profiles modifications create transport barriers, numerical simulations are presented for parameters and profiles taken from the tokamak TCABR. Thus, this paper presents a conceptual investigation rather than detailed comparisons with specific experiments performed in any tokamak.

TCABR's safety factor is described by  $q(r) = 1.0 + 3.0(r/a)^2$ , where  $a$  stands for the plasma radius [23]. We choose to describe the parallel velocity profile as  $v_{\parallel}(r) = -1.43 + 2.82 \tanh(20.3r/a - 16.42)$ , which is a fit chosen from experimental data points, as displayed in Fig. 1b. The equilibrium radial field  $E_r$  was chosen to be non-monotonic according to  $E_r(r) = 3\alpha(r/a)^2 + 2\beta(r/a) + \gamma$ , with  $\alpha = -0.563$ ,  $\beta = 1.250$  and  $\gamma = -1.304$ , and we select from the spectrum analysis an frequency around 10kHz, which gives us  $\omega_0 = 2.673$ . The perturbing electric potential amplitudes  $\phi_n$  are normalized by  $a E_0$ .

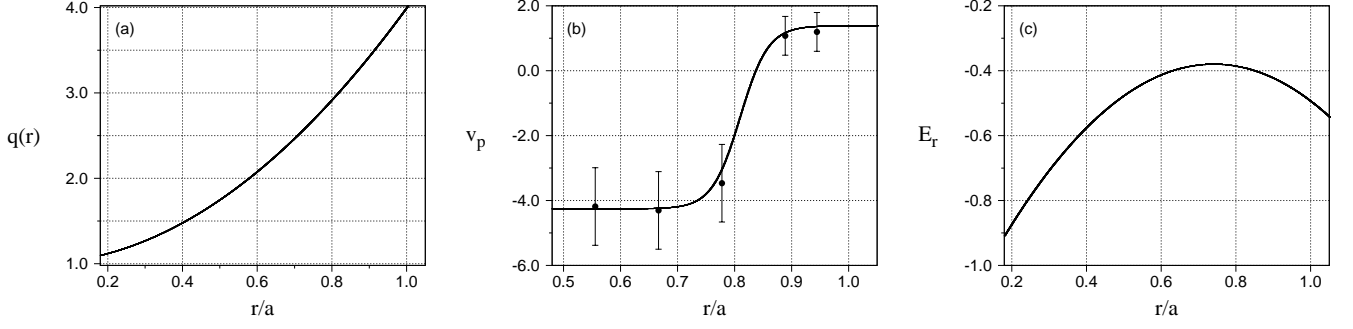


Figure 1. Plasma profiles from tokamak TCABR used in this work. From left to right, we show a typical profile for safety factor  $q(r)$  [23],  $v_{\parallel}$  with experimental data points [7] fitted by a hyperbolic tangent function, and radial electric field profile in equilibrium [24].

The result for the profiles described in Fig. 1 and spatial wave numbers  $M = 16$ ,  $L = 4$ , chosen as typical numbers in the tokamak wave spectrum at plasma edge [13], into Eq. (6) is the resonance profile represented in Fig. 2. Each point of this curve with an integer ordinate identifies a mode  $n$  which is resonant, i.e., which generates islands in the Poincaré section. Not only can we get the mode number, but also the number of centers for each mode and the radial position ( $a\sqrt{I}$ ) of the centers. As seen in Fig. 2, we see that the mode  $n = 3$  has two islands with centers at  $I = (0.27, 1.05)$ , while  $n = 4$  has one center at  $I = 0.21$ . In this way, our study was directed to the interaction of a doublet of same-frequency resonance modes ( $n = 3$ ), a single resonance mode ( $n = 4$ ) and a non-resonant mode ( $n = 2$ ).

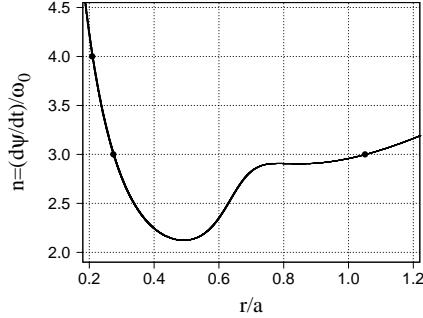


Figure 2. Characteristic curve for resonant modes calculated from Eq.(6) using profiles from Fig. (1). For integer  $n$ , the intersection of the curve with the horizontal lines gives the position of the island center, which characterizes it as a resonant mode. We see that the mode  $n = 3$  has two  $I$  values satisfying the resonance condition, resonant mode  $n = 4$  appears for only one  $I$  value, while  $n = 2$  is not a resonant mode.

To have a clear image on how the chosen modes are superimposed and whether each of them possesses a shearless barrier, the first approach is to see their aspect individually on a Poincaré section and determine the rotation number profile. To see the aspect of perturbing period-two resonant mode  $n = 3$  and its barrier position, we display the numerical solution in Fig. 3a, with the shearless barrier highlighted by a red line (color on-line). Due to the chosen equilibrium profiles, the resonant mode creates islands in two different ranges in phase space determined by the resonance conditions, as presented in Fig. 2. The rotation number profile  $\Omega(I)$  was calculated with initial angle at  $\psi_0 = -\pi$ , as shown in Fig. 3b, and the barrier position is indicated by a red dot (color on-line), the local minimum.

It is known that no islands are present if a mode is non resonant. From a set of invariant lines with the initial action  $I_0$  constant, it is important here to see how “wavy” these invariant lines become in the presence of single frequency, if there is a shearless barrier and where its position on phase space is. The invariant lines of mode  $n = 2$  are depicted on Poincaré section followed by its rotation number in Fig. 4. As before, we detected a local extremum in rotation number, Fig. 4b, characterizing a shearless barrier at  $I = 0.43$  for  $\psi_0 = -\pi$ .

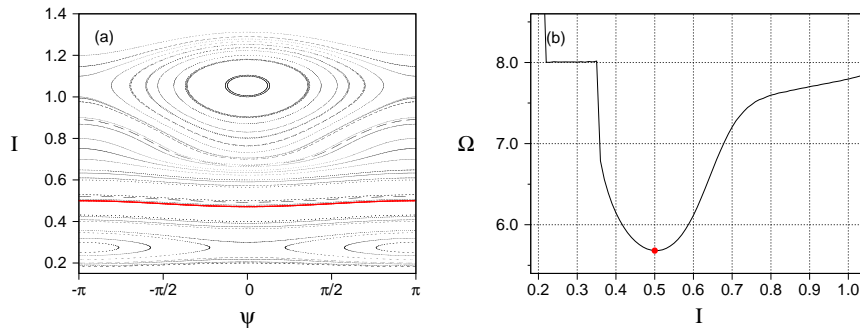


Figure 3. a) Poincaré map for a single resonant mode  $n = 3$  with  $\phi_3 = 1.0 \times 10^{-3}$  (normalized by  $a E_0$ ). The shearless barrier is shown as a red line. In (b) we calculate the rotation number, for which the local minimum stands for the shearless barrier position, which is at  $I = 0.49$ .

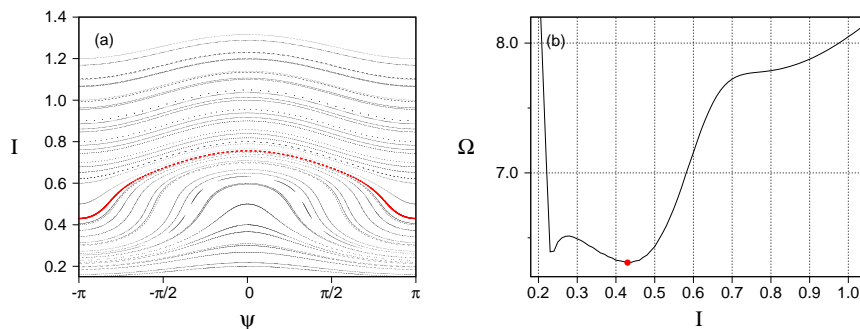


Figure 4. Poincaré portrait for a non-resonant mode  $n = 2$  with  $\phi_2 = 3.6 \times 10^{-3}$  (the perturbing potential  $\phi_2$  is normalized by  $a E_0$ ). The important aspect is to show that, if the mode is not resonant, the contribution of this mode is for barrier formation, which decreases the chaos when more resonant modes are acting on the system.

Having presented the configuration on the Poincaré portrait of a resonant mode of period two and a non resonant and the presence of a shearless barrier on each of them, the next step is to verify the outcome from the non linear interactions between three modes on chaos and on transport barriers formation.

#### IV. NON RESONANT MODE AMPLITUDE

This section discusses the role of the non-resonant mode on chaotic mappings obtained from Eqs (4) and (5) integrated with three modes. With only one resonant mode of period two, we have two islands separated by invariant curves with a shearless barrier, like  $n = 3$  displayed in Fig. 3. Increasing the amplitudes in this kind of system with only one resonant mode generates no visible chaotic region. For chaos to occur, there must be an overlap between two islands of different modes, as in the case of  $n = 3$  and  $n = 4$  where the centers are near, and this effect can be seen on Fig. 5a.

The role of the non resonant perturbation  $n = 2$  is illustrated in Fig. 5b and c. Figure 5b displays a Poincaré section with a combination of three modes,  $n = (2, 3, 4)$ , with amplitudes given by  $\phi_n = (3.6, 1.2, 0.12) \times 10^{-3}$ , amplitudes that correspond to those obtained in spectral analysis on a typical tokamak discharge [22, 25]. The chaos on the Poincaré section results mainly from the overlapping of the modes  $n = 3$  and  $n = 4$ . So the non-resonant mode  $n = 2$  is contributing to spread the chaos over a larger region beyond the overlapping region, which means that the shearless barrier is broken.

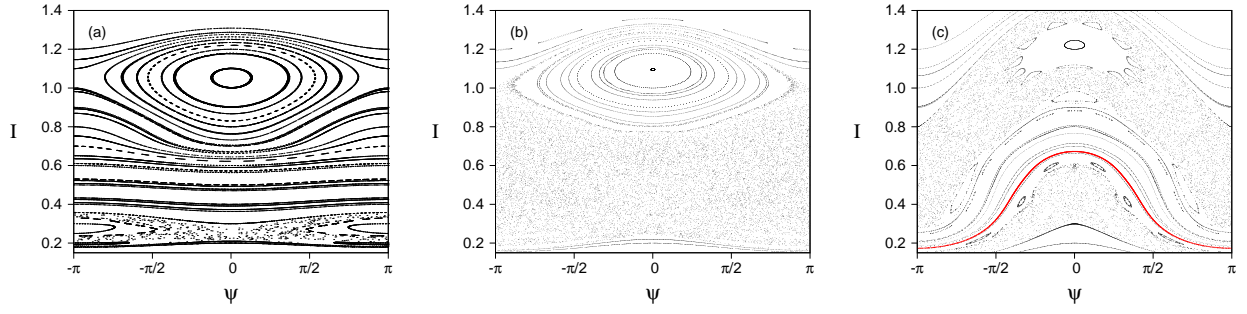


Figure 5. Poincaré sections with three modes  $n = (2, 3, 4)$ . In all panels  $\phi_3 = 1.0 \times 10^{-3}$  and  $\phi_4 = 0.12 \times 10^{-3}$ . On the left panel  $\phi_2 = 0$ , where the chaotic region is delimited by the islands overlapping at  $I \simeq 0.25$ . For  $\phi_2 = 3.6 \times 10^{-3}$ , the middle panel exhibits chaos at  $0.2 < I < 1.0$ . Raising the value of the electric potential for the non-resonant mode  $n = 2$  to  $\phi_2 = 18 \times 10^{-3}$ , the shearless barrier split the chaotic area (on the right panel).

Increasing the non-resonant mode amplitude to  $\phi_2 = 18 \times 10^{-3}$ , the result is a Poincaré map with the chaotic region splitted by a shearless barrier, as seen on Fig. 5c. Making the non-resonant mode a dominant mode, its contribution is to establish the transport barrier and reduce the chaotic area. We want to point out that we can recover the shearless barrier setting  $\phi_2 \sim 4.0 \times 10^{-3}$ ; the large value of  $\phi_2$  was chosen to make clear the structure brought up by the non resonant mode.

In summary, a non-resonant mode can be responsible for broadening the chaotic area and also for the barrier formation. To conclude so, we consider, for the equilibrium profiles of Fig. 1, a combination of two resonant modes  $n = 3$  and  $n = 4$  and a non resonant mode  $n = 2$ , as shown in Fig. 2. For  $\phi_2 = 3.6 \times 10^{-3}$ , the Poincaré map of Fig. 5a shows a resonant island and a chaotic area. However, increasing the non resonant mode amplitude for  $\phi_2 = 18 \times 10^{-3}$ , we get a Poincaré map with a shearless barrier. So, the barrier onset is associated to the increasing of the non resonant mode amplitude. On the other hand, resonant modes create islands and the islands superposition gives rise to a chaotic area between the islands. Thus, the influence of  $n = 2$  on the portrait is to reduce the chaos, and more important, it also reinstates the shearless barrier, indicated by the red curve, dividing the chaotic region in two parts. The higher amplitude perturbation introducing order can be interpreted as a consequence of non-local perturbation introduced by the non-resonant mode  $n = 2$  which alters the global phase space configuration and induces a bifurcation with a shearless curve.

A similar effect has been reported to explain the reversed field pinch stability induced by a non-resonant perturbation in the magnetic field. Namely, in the RFX experiment, a non-resonant perturbation reduced chaos by inducing a bifurcation which modified the phase space configuration, from a multi-helicity to a single helicity state [26, 27]. Another similarity is found in stellarators, as in the Wendelstein 7-X, for which a carefully tailored topology of nested magnetic surfaces needed for good plasma confinement is realized even with magnetic field errors caused by the placement and shapes of the planar coils [28].

## V. INFLUENCE OF THE ELECTRIC FIELD PROFILE

Since the discovery of the L-H transition in ASDEX [29], many theoretical and experimental studies have confirmed the importance of the radial electric field for the formation of internal transport barriers (ITBs) associated with the  $\mathbf{E} \times \mathbf{B}$  velocity shear in magnetic confinement devices [4, 8] (see also references therein). Depending on the equilibrium profiles, small changes on the radial electric field profile may contribute to the transport barriers onset. However, based on the particle guiding-center model proposed in [13], we conjecture that transport barriers may be generated not only due to electric field alterations but rather whenever appears a local shearless condition, depending on the  $q, v_{\parallel}$  profiles.

To illustrate our conjecture, we choose two  $E_r(r)$  profiles presented in Fig. 6a (a different profile from that used in previous sections), with corresponding resonance profiles shown in Fig. 6b, according to its corresponding dash pattern. This small change in the radial electric field is achieved by setting an electrode in which is applied an electric potential difference, as it has been done in TCABR [22, 25]. The most important alteration is that one profile has three resonant modes ( $n = 2, 3, 4$ ), represented by solid blue line, and the other has only two resonant modes ( $n = 3, 4$ ), dashed green line.

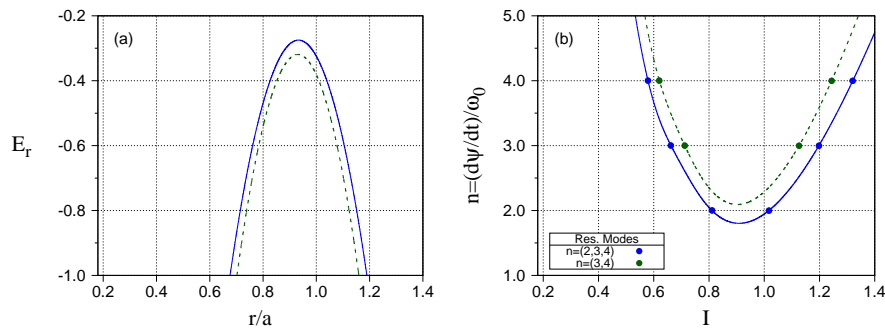


Figure 6. a) Two possible profiles for  $E(r)$ . b) Resonance conditions for profiles shown in (a). One profile has three resonant modes ( $n = 2, 3, 4$ ), represented by solid blue line, and the other has only two resonant modes ( $n = 3, 4$ ), dashed green line.

In Fig. 7, we see how the two resonance conditions modify the Poincaré section. Figure 7a is obtained for three resonant modes profile, while Fig. 7b is obtained for two modes. In Fig. 7b, we can identify a barrier that is created once  $n = 2$  is not anymore a resonant mode. The small change in  $E(r)$  is sufficient to suppress the resonance condition of the  $n = 2$  mode, opening the possibility of a shearless bifurcation seen in Fig. 7b. In this example, the shearless barrier is destroyed if the three modes are resonant, but it is present if the  $n = 2$  becomes non-resonant due to the electric field profile modification. Moreover, this small modification on the  $E_r(r)$  profile can occur during a plasma discharge and produce such a bifurcation with the barrier onset.

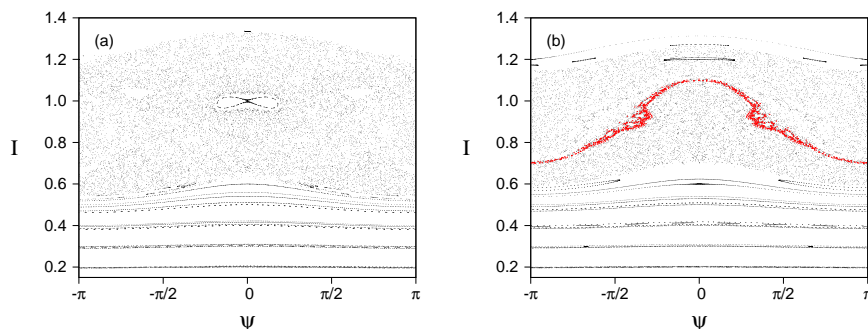


Figure 7. Poincaré section for the two electric field profiles given by V with electric potential  $\phi_n = (5.9, 1.2, 0.12) \times 10^{-3}$ .  $n = (2, 3, 4)$ . In (a) the three modes are resonant, while in (b) only  $n = 2$  is a not resonant mode.

In general, the electrostatic turbulence consists of a broadband spectra with a mixing of resonant and non-resonant modes. We show here that some of the 3 base modes may affect the existence of barriers once they are sensitive to small changes in the electric field profile.

## VI. CONCLUSIONS

In our investigation, we apply a model, described by a two-dimensional symplectic drift map proposed to numerically integrate orbits on the long transport time scales, avoiding long integration times of the differential equations typically found for the exact guiding-center orbits in tokamaks. For typical tokamak equilibrium profiles and spectral potential, we determine the wave resonance conditions. As expected, the chaotic region and the particle transport in phase space depend on the resonant wave amplitudes and the equilibrium shear determined by the magnetic, electric field and velocity profiles. Within this model we show numerical examples of the shearless barrier onset that may occur during the tokamak discharges.

First we show how the increasing of a non-resonant wave amplitude can create a shearless transport barriers. This occurs because increasing the non-resonant wave amplitude modifies the phase space and induces a bifurcation with a shearless curve.

After that, we investigate the triggering of shearless particle transport barriers in tokamaks as a consequence of modifications on the plasma equilibrium profiles compatible with those commonly observed in tokamaks. Our results indicate that this barrier triggering could be commonly observed in tokamaks.



We conjecture that the examples of shearless barrier onset could be observed in some tokamak discharges during which the wave amplitudes and the equilibrium shear are spontaneously slightly modified.

## ACKNOWLEDGMENTS

The authors thank the financial support from the Brazilian Federal Agencies CNPq, grants No. 457030/2014-3 and N° 446905/2014-3, PNPd CAPES Program, and the São Paulo Research Foundation (FAPESP, Brazil) under grants No. 2011/19296-1 and N° 2015/16471-8. YE enjoyed the hospitality of the plasma physics and oscillations control group of the University of São Paulo and support from CAPES-COFECUB grant Ph 908/18. ILC thanks the hospitality during his stay at Aix-Marseille Université. We thank Prof. D. Escande for his suggestions.

- 
- [1] Cavedon, M.; Pütterich, T.; Viezzer, E. *et al.* Nuclear Fusion, **57**(1):014002, 2017.
  - [2] Horton, W. *Turbulent Transport in Magnetized Plasmas*. WORLD SCIENTIFIC, 2nd edition, 2018. ISBN 978-981-3225-88-6.
  - [3] Wolf, R. C. Plasma Physics and Controlled Fusion, **45**(1):R1, 2003.
  - [4] Connor, J.; Fukuda, T.; Garbet, X. *et al.* Nuclear Fusion, **44**:R1–R49, 2004.
  - [5] Garbet, X.; Mantica, P.; Angioni, C. *et al.* Plasma Physics and Controlled Fusion, **46**(12B):B557, 2004.
  - [6] Viezzer, E.; Pütterich, T.; Conway, G. *et al.* Nuclear Fusion, **53**(5):053005, 2013.
  - [7] Severo, J.; Nascimento, I.; Kuznetsov, Y. *et al.* Nuclear Fusion, **49**(11):115026, 2009.
  - [8] Burrell, K. H. Physics of Plasmas, **4**(5):1499, 1997.
  - [9] Constantinescu, D. and Constantinescu, R. Physica Scripta, (4):244, 2005.
  - [10] Caldas, I. L.; Viana, R. L.; Abud, C. V. *et al.* Plasma Physics and Controlled Fusion, **54**(12):124035, 2012.
  - [11] del Castillo-Negrete, D.; Greene, J. and Morrison, P. Physica D: Nonlinear Phenomena, **91**(1):1 – 23, 1996.
  - [12] Szezech, J. D.; Caldas, I. L.; Lopes, S. R. *et al.* Chaos: An Interdisciplinary Journal of Nonlinear Science, **19**(4):043108, 2009.
  - [13] Horton, W.; Park, H.-B.; Kwon, J.-M. *et al.* Physics of Plasmas, **5**(11):3910–3917, 1998.
  - [14] Ferro, R. and Caldas, I. Physics Letters A, **382**(15):1014 – 1019, 2018.
  - [15] Marcus, F. A.; Caldas, I. L.; Guimarães-Filho, Z. O. *et al.* Physics of Plasmas, **15**(11):112304, 2008.
  - [16] Escande, D. Physics Reports, **121**:165–261, 1985.
  - [17] H., W.; Teukolsky, S. A.; Vetterling, W. T. *et al.* *Numerical Recipes 3rd Edition: The Art of Scientific Computing*. Cambridge University Press, New York, NY, USA, 3 edition, 2007. ISBN 0521880688, 9780521880688.
  - [18] Farazmand, M.; Blazeovski, D. and Haller, G. Physica D: Nonlinear Phenomena, **278-279**:44 – 57, 2014.
  - [19] Szezech, J. D.; Caldas, I. L.; Lopes, S. R. *et al.* Physical Review E - Statistical, Nonlinear, and Soft Matter Physics, **86**(3):1–8, 2012.
  - [20] Del-Castillo-Negrete, D. Physics of Plasmas, **7**(5):1702, 2000.
  - [21] Morrison, P. J. Physics of Plasmas, **7**(6):2279–2289, 2000.
  - [22] Nascimento, I.; Kuznetsov, Y.; Severo, J. *et al.* Nuclear Fusion, **45**(8):796–803, 2005.
  - [23] Fernandes, T. *Instabilidades MHD no tokamak TCABR*. Ph.D. thesis, IF-USP, 2016.
  - [24] Rosalem, K.; Roberto, M. and Caldas, I. Nuclear Fusion, **54**(6):064001, 2014.
  - [25] Nascimento, I.; Kuznetsov, Y.; Guimarães-Filho, Z. *et al.* Nuclear Fusion, **47**(11):1570–1576, 2007.
  - [26] Escande, D. F.; Paccagnella, R.; Cappello, S. *et al.* Phys. Rev. Lett., **85**:3169–3172, 2000.
  - [27] Lorenzini, R.; Martines, E.; Piovesan, P. *et al.* Nature Physics, **5**(8):570–574, 2009.
  - [28] Pedersen, T. S.; Otte, M.; Lazerson, S. *et al.* Nature Communications, **7**:13493 EP –, 2016. Article.
  - [29] Wagner, F.; Becker, G.; Behringer, K. *et al.* Physical Review Letters, **49**(19):1408–1412, 1982.